Suppression of the Rayleigh-Taylor Instability due to Self-Radiation in a Multiablation Target

Shinsuke Fujioka,[1,*] Atsushi Sunahara,[1] Katsunobu Nishihara,[1] Naofumi Ohnishi,[2] Tomoyuki Johzaki,[1]
Hiroyuki Shiraga,[1] Keisuke Shigemori,[1] Mitsuo Nakai,[1] Tadashi Ikegawa,[1] Masakatsu Murakami,[1] Keiji Nagai,[1]
Takayoshi Norimatsu,[1] Hiroshi Azechi,[1] and Tatsuhiko Yamanaka[1]
[1]*Institute of Laser Engineering, Osaka University, 2-6 Yamada-Oka, Suita, Osaka, 565-0871 Japan*
[2]*Department of Aeronautics and Space Engineering, Tohoku University 01 Aramaki-Aza-Aoba, Aoba-ku, Sendai, 980-8579 Japan*
(Received 3 November 2002; published 13 May 2004)

A scheme to suppress the Rayleigh-Taylor instability has been investigated for a direct-drive inertial fusion target. In a high-Z doped-plastic target, two ablation surfaces are formed separately—one driven by thermal radiation and the other driven by electron conduction. The growth of the Rayleigh-Taylor instability is significantly suppressed on the radiation-driven ablation surface inside the target due to the large ablation velocity and long density scale length. A significant reduction of the growth rate was observed in simulations and experiments using a brominated plastic target. A new direct-drive pellet was designed using this scheme.

DOI: 10.1103/PhysRevLett.92.195001 PACS numbers: 52.35.Py, 52.50.Jm, 52.57.Fg, 52.70.La

In an inertial fusion energy (IFE) target [1], a lower-density plasma corona accelerates a massive fuel plasma inward. The ablation surface between the two regions is unstable to the Rayleigh-Taylor (RT) instability [2]. Perturbations on the ablation surface caused by nonuniform laser irradiation and/or initial imperfections of its surface grow exponentially, which may reduce energy gain from the target. The RT instability has been recognized as a critical problem to be overcome toward the goal of IFE. Experimental [3] and theoretical [4] research on the RT instability has been diligently conducted.

The growth of the RT instability in an IFE target is stabilized by ablation. The growth rate $\gamma(k)$ is represented by $\gamma(k) = \alpha\sqrt{kg/(1 + kL_{\mathrm{m}})} - \beta k V_{\mathrm{a}}$ [5,6], where α and β are constants depending on the structure of the ablation surface [6], k is the wave number of the perturbation, g is the acceleration, L_{m} is the minimum density scale length at the ablation surface, and V_{a} is the ablation velocity that is given by the mass ablation rate per unit surface area $\dot{m}$ divided by the ablation density ρ_{a}: $V_{\mathrm{a}} = \dot{m}/\rho_{\mathrm{a}}$. In the indirect-drive approach [5], once laser energy is converted into x-ray radiation in a hohlraum, the mass ablation rate is generally much larger than that in the direct-drive approach. The higher mass ablation rate results also in a longer density scale length. The growth in the indirect drive is thus generally much less than that in the direct drive. Nevertheless, the direct-drive approach is more attractive due to its simplicity and higher coupling efficiency from the laser energy to the kinetic energy of the imploding shell [7].

In the direct-drive approach, several schemes to suppress the RT instability [8–11] have been proposed for the National Ignition Facility (NIF) [12] and a laser fusion power plant. In this Letter, we investigated a RT suppression scheme, "SMART" (stabilization of the RT instability by multiablation in a self-radiation target), which accounts for the radiation drive in a simple direct-drive target, and proposed a new pellet design based on this SMART scheme. When a high-Z material is doped in a direct-drive plastic target, which we call a self-radiation target, radiation emitted from the high-temperature plasma corona generates a new ablation ahead as shown in Fig. 1. One of the ablation fronts is formed due to electron conduction [13] and the other is due to thermal radiation [14]. We will show theoretically and experimentally that the multiablation structure leads to the suppression of the RT instability, because of the larger ablation velocity and the longer density scale length. All experiments were performed in a planar geometry as a small solid angle component of a spherical target. A brominated plastic (CHBr: $C_{50}H_{47}Br_3$) is chosen as the self-radiation target.

Figure 1 shows spatial profiles of mass density ρ, electron temperature T_{e}, and radiation brightness temperature T_{r} in CHBr and polystyrene (CH) targets

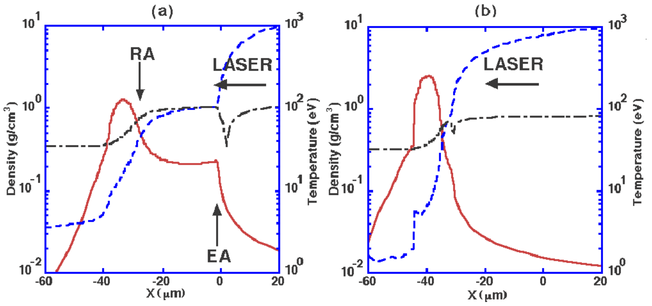

FIG. 1 (color online). 1D simulated profiles of mass density (solid lines), electron temperature (dashed lines), and radiation brightness temperature (dash-dotted lines) in CHBr (a) and CH (b) targets at 1.2 ns after the onset of the main laser pulse. The origin of space is set to be the initial position of the target rear surface. RA and EA in (a) indicate radiation-driven ablation surface and electron-driven ablation surface, respectively.

calculated with a 1D hydrodynamic simulation code (ILESTA-1D) [15]. The code includes multigroup diffusion approximated radiation transport (radiation energy from 0.05 to 3.0 keV is divided into 100 groups), the average atom model in the collisional-radiative equilibrium, and an equation of state based on the Thomas-Fermi model with the bounding correction [16]. This code was benchmarked carefully in experiments relevant to direct- [17] and indirect-drive approaches [18]. In the simulation, the laser is a flattop pulse (intensity of $I_L = 1.0 \times 10^{14}$ W/cm^2, wavelength of $\lambda_L = 0.35$ μm, and pulse duration of $\tau_L = 2.5$ ns) with a foot pulse ($I_L = 1.0 \times 10^{12}$ W/cm^2, $\lambda_L = 0.53$ μm, and $\tau_L = 2.0$ ns). The target thickness was set to be 25 μm for both targets. The initial densities of CHBr and CH targets are 1.26 and 1.06 g/cm^3, respectively.

As shown in Fig. 1(a), the radiation-driven ablation (RA) front is formed ahead of the electron-driven ablation (EA) front. Furthermore, a density plateau of approximately 0.2 g/cm^3 appears between the two ablation fronts. Since the two ablation fronts propagate with different velocities, the plateau region extends in time. The local thermal equilibrium (LTE) condition is approximately satisfied in the plateau plasma. Because the radiation generated near the EA front propagates diffusively through a LTE plasma, nonuniformity of the laser irradiation is expected to be thermal smoothed out before it transmits to the RA front. As shown in Figs. 1(a) and 1(b), the peak density of the plasma in the CHBr target is lower than that in the CH target because of preheat caused by a high energy component of the self-emitted radiation. And the flight distance of the CHBr target is slightly shorter than that of the CH target. An analysis considering time dependence of the mass ablation rate and acceleration shows the kinetic energy in the CHBr target is 30% less than that of the CH target. Note that this multiablation structure was previously found in simulations [19,20].

The RT growth under such a complex multiablation structure was investigated with a 2D Eulerian radiation hydrodynamic code (RAICHO) [21]. The RAICHO code includes almost the same physical models in the ILESTA-1D code, except the assumptions of one-temperature plasma and an equation of state for an ideal gas. The code uses Cartesian grids whose spatial resolution is 0.25 μm. The laser was assumed to be normally incident on the target and the laser absorption was calculated with 1D ray tracing. The target and the laser conditions are the same as those of the 1D simulations. Wavelength and amplitude of the perturbation imposed initially on the target surface is 80 and 0.8 μm, respectively. It is clearly seen in Fig. 2(a) that the perturbation predominantly grows at the RA surface, while the EA surface remains without any substantial deformation. On the other hand, the deformation of both the ablation surface and the rear surface of the CH target is much larger than that of the CHBr target. The linear RT growth rate of the CHBr target is strongly suppressed to be $\gamma = 0.79$ ns^{-1} in the 2D simulation, while that of the CH is $\gamma = 1.7$ ns^{-1}.

To investigate the physical mechanism of the suppression of the RT growth, the linear growth rate of the RT instability was evaluated theoretically using the Betti-Goncharov procedure [6], which uses the parameters (the Froude number Fr, the power index of the thermal conduction ν, and the ablation scale length L_0, g, L_m, and V_a) obtained from the 1D simulation. Those parameters are tabulated in Table I. We evaluated the RT growth rate only at the RA front, since the perturbations at the EA front are predicted to be almost stable because of $\nabla\rho \cdot \nabla p > 0$ (p: pressure) in the 1D simulation. The ablation velocity $\langle V_a \rangle$ of the CHBr target is 3 times larger than that of the CH target, where $\langle\,\rangle$ represents the averaged value from 1.5 to 2.0 ns after the onset of the main laser pulse. A larger mass ablation rate and a longer density scale length are observed in the CHBr target compared with those in the CH target. The evaluated linear RT growth rates for the wavelength of 80 μm are $\gamma = 1.1$ ns^{-1} for the CHBr target and $\gamma = 1.8$ ns^{-1} for the CH target. These values agree fairly well with the growth rates observed in the 2D simulation.

We performed experiments at the GEKKO XII-HIPER (High Intensity Plasma Experimental Research) laser facility [22] to confirm the validity of the SMART scheme. In the GEKKO XII-HIPER system, nine frequency-tripled ($\lambda_L = 0.35$ μm, $\tau_L = 2.5$ ns) laser beams with two-dimensional smoothing by spectral dispersion [23] were used for driving the target uniformly, while the other three beams of frequency-doubled ($\lambda_L = 0.53$ μm, $\tau_L = 2.0$ ns) partially coherent light [24] were used as a foot pulse for precompression of the targets. Main and foot beams are the flattop pulses. All lasers were implemented with kinoform phase plates [25] to obtain profile-controlled uniform laser illumination. The composition of the CHBr target used in the experiment was $C_{50}H_{41.5}Br_{3.3}$, and its initial density was 1.35 g/cm^3.

First of all, we measured a trajectory of the rear surface of a laser-driven CHBr target with side-on x-ray

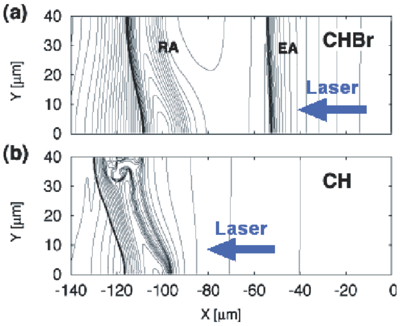

FIG. 2 (color online). 2D simulated density contours of CHBr (a) and CH (b) targets at 1.9 ns after the beginning of the main laser pulse. The contour lines are drawn at isodensity of 40 levels increasing logarithmically from 10^{-2} to 10^{1} g/cm^3.

TABLE I. Parameters determining linear RT growth rate

	Fr	ν	L_0 (μm)	L_m (μm)	V_a (cm/s)	g (cm/s^2)	ρ_a (g/cm^3)	$\dot{m}$ (g/cm^2 s^{-1})	α	β
CH	0.04	0.67	0.42	1.3	9.2×10^4	5.0×10^{15}	3.0	2.7×10^5	1.0	1.9
CHBr	0.20	0.93	0.99	3.7	3.0×10^5	4.5×10^{15}	1.5	4.6×10^5	0.9	1.5

backlighting. The rear surface of the target is probed from the side by an x ray, and its radiograph is imaged on an x-ray streak camera. Figure 3 shows the trajectories obtained in the experiment and simulation. In this shot, CHBr with an initial thickness of 25 μm was used and laser intensities of foot and main pulses were 5.0×10^{11} W/cm^2 and 4.0×10^{13} W/cm^2, respectively. The simulation code predicts fairly well the motion of the rear surface observed in the experiment. Therefore the code is expect to predict overall hydrodynamics of the laser-driven CHBr target.

Planar CHBr and CH targets, whose surfaces were initially corrugated with single-mode sinusoidal perturbation, were irradiated by a laser, and face-on backlit by 1.5 keV x rays emitted from a zinc plasma. For observing growth of areal-mass-density perturbation, the radiograph was made on an x-ray streak camera with a slit imager, whose slit was 10 μm in width and in parallel to ridges and valleys of the perturbations. The camera's magnification was 26. The modulation transfer function of the diagnostic system was evaluated from an x-ray backlit grid image in a separate shot and was used in the analysis. Temporal resolution of the system was 200 ps. Sinusoidal perturbation with wavelength of 25 μm and amplitude of 0.3 μm was imposed on the laser-irradiation side of 18 μm-thick CHBr targets by using the Fourier laser machining. On the other hand, perturbation with wavelength of 20 μm and amplitude of 0.2 μm was imposed on the 25 μm-thick CH targets.

Figure 4 shows the streaked x-ray radiographs of perturbed CHBr (a) and CH (b) targets. In these RT shots, the intensities of foot and main pulses are 1.0×10^{12} W/cm^2 and 1.5×10^{14} W/cm^2, respectively. Temporal evolutions of growth factors of the areal density perturbations are shown in Fig. 4(c). The growth factor is defined as the areal density perturbation [$\delta(\rho l)$] divided by its initial value. The significant growth of the areal density perturbation was not observed in the CHBr target within our experimental resolution, while the growth rate of the perturbation in the CH target is 2.6 ± 0.3 ns^{-1}.

The theoretical linear growth rate for the CHBr target is calculated to be 1.5 ns^{-1} using the parameters: $\mathrm{Fr} = 0.2$, $L_0 = 0.86$ μm, $\nu = 0.85$, $g = 7.9 \times 10^{15}$ cm/s^2, and $V_a = 3.6 \times 10^5$ cm/s. Those are evaluated from a 1D simulation with the experimental conditions. The evaluated growth rate in the CHBr target is large enough to amplify the perturbation to be observable. This disagreed with the experimental observation. The strong suppression of the RT growth in the CHBr target may be explained by the reduction of a nonlinear transition amplitude of the linear RT growth. The weakly nonlinear theory [26] predicts that the nonlinear transition amplitude, at which the RT growth begins to be affected by nonlinearity of hydrodynamics, is reduced strongly by the laser ablation especially for perturbation wavelength neighboring the RT cut-off one. We have evaluated the transition amplitudes by applying the theory with the parameters above. The transition amplitude in the CHBr target is reduced by the enhanced ablative stabilization to

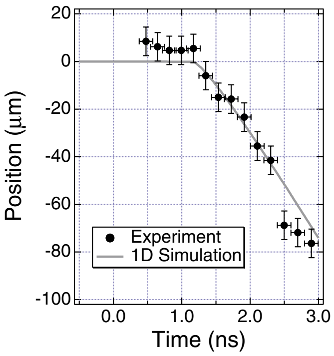

FIG. 3 (color online). Target trajectories observed in the experiment (circles) and simulation (solid gray line). The origins of time and space are set to be the onset of the main laser irradiation and the initial position of the rear surface of the target.

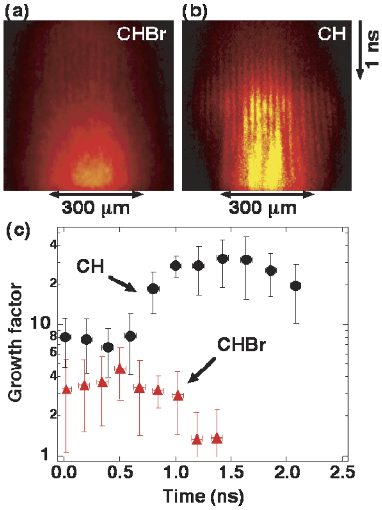

FIG. 4 (color online). Face-on x-ray radiographs of laser driven perturbed CHBr (a) and CH (b) targets. (c) The temporal evolution of the areal density perturbation in CHBr (triangles) and CH (circles) targets. The origin of the time is set to be the time of onset of the main laser drive.

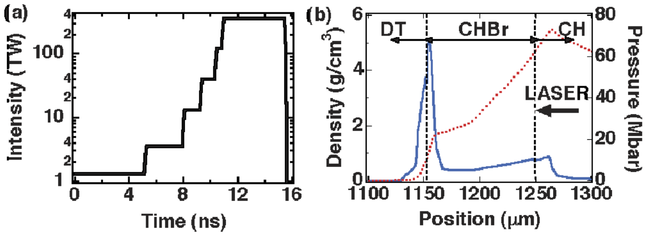

FIG. 5 (color online). Pulse shape of the incident laser (a). 1D simulated profile of density (solid line) and pressure (dotted line) at 14 ns (b). Broken lines in (b) indicate interfaces of DT-CHBr and CHBr-CH.

be 0.76 μm, which is 5 times smaller than that in the CH target (4.0 μm). We have performed 2D simulations with the same laser and target conditions as the experimental ones. The 2D simulation also shows that the RT growth in the CHBr target is suppressed not to be observable. Therefore, we concluded that the RT growth in the CHBr transitted into the nonlinear phase at early time, so that the RT growth became smaller than that predicted by the linear theory, and the significant RT growth was not observed in the experiment.

Lastly, we describe a new pellet [27] designed for the direct-drive NIF experiment using this scheme. The pellet is multilayered, which consists of a 0.1 μm-thick Au overcoat, a 15 μm-thick CHBr ablator, a 13 μm-thick CH ablator, a 28 μm-thick CHBr ablator, and a 70 μm-thick DT-ice fuel layer. The radius of the shell is 1750 μm and the shell is filled with 0.3 mg/cm^3 deuterium-tritium (DT) gas. The thin Au layer is overcoated for enlarging the stand-off distance to reduce the imprint caused by nonuniform laser illumination [10]. The multilayered (CHBr/CH/CHBr) ablator is used to obtain sufficient implosion velocity and also to prevent the formation of an internal RT unstable interface between the ablator and the fuel. The pulse shape of the incident laser shown in Fig. 5(a) has five steps to keep low adiabat of the DT fuel layer. The total energy of the incident laser is 1.8 MJ. As shown in Fig. 5(b), the ILESTA-1D code predicts that the multiablation structure is formed inside the multilayered ablator throughout laser irradiation; therefore growth of the perturbation on the EA and the RA fronts is suppressed by the mechanism discussed above. Furthermore, the interface between the CHBr ablator and the DT fuel layer is predicted to be RT stable during the acceleration phase, because mass density of the CHBr ablator is larger than that of the DT fuel layer. The pellet is predicted to ignite and produce 41 MJ of thermonuclear energy.

In conclusion, we have investigated a scheme to suppress the RT instability using the self-radiation target, in which the multiablation structure is formed. The RT instability is stabilized by the large ablation velocity and the long density scale length due to the radiation drive. The stabilization was clearly observed in the 2D simulations and the experiment. Although further implosion experiments and 2D calculations in a spherical geometry are required, the SMART scheme appears to be an attractive candidate for the pellet design.

The authors would like to thank the staff at the Institute of Laser Engineering, Osaka University. Computations were carried out on NEC SX-5 at Cybermedia Center, Osaka University.

---

*Electronic address: sfujioka@ile.osaka-u.ac.jp

[1] J. Nuckolls *et al.*, Nature (London) **239**, 139 (1972).
[2] S. Chandrasekhar, *Hydrodynamic and Hydromagnetic Stability* (Oxford University Press, London, 1968).
[3] K. Shigemori *et al.*, Phys. Rev. Lett. **78**, 250 (1997); S. G. Glendinning *et al.*, *ibid.* **78**, 3318 (1997); C. J. Pawley *et al.*, Phys. Plasmas **6**, 565 (1999); J. P. Knauer *et al.*, *ibid.* **7**, 338 (2000).
[4] S. E. Bodner, Phys. Rev. Lett. **33**, 761 (1974); H. Takabe *et al.*, Phys. Fluids **28**, 3676 (1985); J. Sanz, Phys. Rev. Lett. **73**, 2700 (1994); V. N. Goncharov *et al.*, Phys. Plasmas **3**, 4665 (1996); A. R. Pritz *et al.*, *ibid.* **4**, 1117 (1997).
[5] J. Lindl, Phys. Plasmas **2**, 3933 (1995).
[6] R. Betti *et al.*, Phys. Plasmas **5**, 1446 (1998).
[7] S. E. Bodner *et al.*, Phys. Plasmas **5**, 1901 (1998).
[8] J. D. Lindl and W. C. Mead, Phys. Rev. Lett. **34**, 1273 (1975).
[9] P. W. McKenty *et al.*, Phys. Plasmas **8**, 2315 (2001); V. N. Goncharov *et al.*, *ibid.* **10**, 1906 (2003).
[10] S. E. Bodner *et al.*, Phys. Plasmas **7**, 2298 (2000).
[11] K. Shigemori *et al.*, Bull. Am. Phys. Soc. **46**, 281 (2001).
[12] M. D. Campbell and W. J. Hogan, Plasma Phys. Controlled Fusion **41**, B39 (1999).
[13] H. Takabe, K. Nishihara, and T. Taniuti, J. Phys. Soc. Jpn. **45**, 2001 (1978).
[14] K. Nishihara, Jpn. J. Appl. Phys., Part 1, **21**, L571 (1982).
[15] H. Takabe *et al.*, Phys. Fluids **31**, 2884 (1988).
[16] R. M. More *et al.*, Phys. Fluids **31**, 3059 (1988).
[17] H. Azechi *et al.*, Phys. Plasmas **4**, 4079 (1988).
[18] H. Nishimura *et al.*, Phys. Rev. A **43**, 3073 (1991).
[19] *LLE Review Quarterly Report* (University of Rochester, New York, 1990), Vol. 43, p. 117.
[20] J. P. Dahlburg *et al.*, J. Quant. Spectrosc. Radiat. Transfer **54**, 113 (1995); G. Hazak *et al.*, Phys. Plasmas **6**, 4015 (1999).
[21] N. Ohnishi *et al.*, J. Quant. Spectrosc. Radiat. Transfer **71**, 551 (2001).
[22] N. Miyanaga *et al.*, in *Proceedings of the 18th International Conference on Fusion Energy* (IAEA, Sorrento, Italy, 2001) (IAEA Report No. IAEA-CN-77, 2000).
[23] S. Skupsky *et al.*, J. Appl. Phys. **66**, 3456 (1989).
[24] H. Nakano *et al.*, Appl. Phys. Lett. **63**, 580 (1993).
[25] S. N. Dixit *et al.*, Opt. Lett. **19**, 417 (1994).
[26] T. Ikegawa and K. Nishihara, Phys. Rev. Lett. **89**, 115001 (2002).
[27] A. Sunahara *et al.*, in Proceedings of Inertial Fusion Science and Application, 2003 (to be published).